Materials Advances

ROYAL SOCIETY OF CHEMISTRY

PAPER

View Article Online
View Journal | View Issue

Cite this: *Mater. Adv.*, 2025, **6**, 6528

Unveiling the role of silver-promoted phase evolution in antimony sulfide thin films for photoelectrochemical activity

D. M. Kavya, [a] Akshay Kumar Sonwane,[b] Y. N. Sudhakar, [c] Sajan D. George [d] and Y. Raviprakash *[a]

Received 9th June 2025,
Accepted 30th July 2025

DOI: 10.1039/d5ma00616c

rsc.li/materials-advances

Antimony sulfide (Sb_2S_3) is a promising candidate for photoelectrochemical (PEC) water splitting due to its narrow band gap (~1.7 eV), high optical absorption coefficient, and the earth-abundant nature of its constituent elements. However, deep-level defects promoting charge carrier recombination often hinder PEC performance. In this study, we investigated the effects of silver (Ag) incorporation on the structural, morphological, and photoelectrochemical properties of thermally evaporated Sb_2S_3 thin films. Compared with pristine films, Ag doping induces a shift in the preferred crystallographic orientation from (*hk*0) to (*hk*1), with notable morphological modifications and a reduction in surface roughness. Despite these structural improvements, the photocurrent density of the Ag-doped films decreased from 0.49 to 0.27 mA cm^{-2} under standard illumination, indicating that Ag incorporation adversely affects charge transport and catalytic activity. These findings highlight the critical role of dopant-induced defects in governing the PEC performance of Sb_2S_3-based photoelectrodes.

1. Introduction

Antimony(III) sulfide (Sb_2S_3) has garnered considerable attention as a promising photocathode material for photoelectrochemical (PEC) water splitting due to its distinctive optoelectronic properties. It possesses a narrow optical bandgap of approximately 1.7 eV and a high absorption coefficient of 10^4–10^5 cm^{-1} for photons with energies above the bandgap, making it suitable for efficient solar energy absorption.[1–5] Additionally, Sb_2S_3 offers a high theoretical photocurrent density of ~24.5 mA cm^{-2} and a solar-to-hydrogen (STH) conversion efficiency of up to 28%, further highlighting its potential for sustainable hydrogen generation.[6] Despite these advantages, the practical application of Sb_2S_3 in PEC devices is hindered by several limitations. In thin films, inadequate thickness and material density can lead to insufficient light absorption and interference effects. Conversely, thicker films often suffer from inhomogeneity, increased internal scattering, and stress-induced defects, which collectively reduce the overall device performance.[7,8]

Elemental doping has been investigated as a viable method to modify the electrical and structural characteristics of Sb_2S_3 to overcome these obstacles.[9–13] Sn-doped Sb_2S_3 thin films were found to be polycrystalline, with solid grains and phase changes observed at higher Sn concentrations. Optical studies revealed a direct band gap in the range of 1.45–1.80 eV and a refractive index between 3.38 and 6.39.[14] Copper (Cu) doping in Sb_2S_3 thin films *via* a co-evaporation route has improved crystallinity by enhancing grain size and promoting vertical orientation. The electrical conductivity increased from 1.28×10^{-8} to 1.20×10^{-7} S cm^{-1}, while the trap state density decreased from 1.05×10^{15} to 1.74×10^{15} cm^{-3}. A slight upshift in valence band energy confirmed improved carrier concentration and hole extraction. As a result, the power conversion efficiency (PCE) increased from 4.18% to 4.61%, with an increase in open-circuit voltage from 0.622 V to 0.637 V.[15] Among various dopants, silver (Ag) has demonstrated particular promise due to its favorable ionic radius. The ionic radius of Ag^+ (~1.15 Å) is similar to that of Sb^{3+}, allowing it to integrate smoothly into the Sb_2S_3 crystal lattice without causing structural distortion. This compatibility facilitates the incorporation of Ag^+ through intercalation, leading to improved electrical conductivity, enhanced charge transport, and greater structural stability. Additionally, the electronic configuration of Ag^+ supports its effective integration into the Sb_2S_3 matrix. As a result, Ag doping is expected to influence crystallinity, reduce defect density, and improve charge transport properties,

[a] *Department of Physics, Manipal Institute of Technology, Manipal Academy of Higher Education, Manipal-576104, India. E-mail: raviprakash.y@manipal.edu*
[b] *Department of Metallurgical Engineering & Materials Science (MEMS), Indian Institute of Technology, Indore – 453552, India*
[c] *Department of Chemistry, Manipal Institute of Technology, Manipal Academy of Higher Education, Manipal, 576104, Karnataka, India*
[d] *Centre for Applied Nanosciences, Manipal Institute of Applied Physics, Manipal Academy of Higher Education, Manipal-576104, Karnataka, India*

thereby enhancing the photoelectrochemical (PEC) performance of the Sb_2S_3-based material.[16] Furthermore, co-doping Ag^+ and Cu^+ into Sb_2S_3 films *via* electrophoretic deposition (EPD), followed by post-annealing at 300 °C, resulted in crystalline films with enhanced conductivity and photocurrent response.[16] The formation of secondary phases such as $AgSbS_2$ and $CuSbS_2$ was observed without detectable metallic or oxide impurities, and Ag doping was found to reduce the crystallization temperature while slightly tuning the bandgap, resulting in a value of approximately 1.73 eV.[16] Structural and XPS analyses confirmed the incorporation of Ag, which resulted in a reduced crystallite size, increased lattice strain, and enhanced visible-light activity. The conductivity of the Sb_2S_3 films increased from 1.84×10^{-9} to 1.33×10^{-8} $(\Omega\ cm)^{-1}$ after Ag doping, indicating improved charge transport properties.[17] Notably, the Mo/Ag:Sb_2S_3/CdS/Pt photocathode achieved a photocurrent density of 9.4 mA cm^{-2}, illustrating the performance benefits of Ag incorporation. Films fabricated by sulfurizing Ag/Sb bimetallic precursors *via* dual-source electron beam evaporation resulted in the formation of $AgSbS_2$ units and [*hk*1]-oriented Sb_2S_3 crystals. This preferred orientation suppressed [*hk*0] stacking faults, leading to films with lower defect densities, enhanced conductivity, and improved carrier mobility. The engineered crystallographic orientation significantly increased the charge separation and injection efficiencies, highlighting the potential of orientation-controlled Ag doping strategies for high-efficiency Sb_2S_3-based PEC devices.[18]

In this study, Ag-doped Sb_2S_3 (Ag:Sb_2S_3) thin films were employed, for the first time, as bare photoanodes for photoelectrochemical (PEC) water-splitting applications. Unlike prior reports where Sb_2S_3 primarily served as a photocathode or required complex heterostructures, our work demonstrated its direct applicability as a standalone photoanode upon Ag incorporation. By systematically varying the Ag doping concentration, we successfully induced a preferential [*hk*1] crystallographic orientation in Sb_2S_3 films, which is known to promote efficient charge separation and transport. When Sb_2S_3 films exhibit a predominantly parallel orientation relative to the substrate, stacking along the [*hk*0] direction through weak van der Waals interactions, the resulting PEC performance is limited. This is primarily due to inefficient charge transport caused by interchain or interlayer hopping of photogenerated carriers. In contrast, a mixed orientation that includes vertical growth along the [*hk*1] direction, where chains are interconnected by strong covalent Sb–S bonds, facilitates more efficient intra-ribbon carrier transport and significantly reduces recombination losses. This favorable crystallographic alignment leads to enhanced PEC performance in Ag-doped Sb_2S_3 films.[6]

A thorough grasp of how Ag doping affects the structural, morphological, optical, and electrochemical properties of Sb_2S_3 films is provided by this work. While previous studies have reported increased surface roughness and photocurrent densities due to Ag incorporation, our findings extend this knowledge by correlating these studies with changes in surface wettability, optical absorption, and interface defects that are critical for optimizing the PEC water splitting efficiency. The observed improvements in the linear sweep voltammetry (LSV) response and overall PEC performance are attributed to enhanced light harvesting, improved charge carrier mobility, and reduced recombination losses due to Ag-induced lattice modifications and crystallographic alignment.

2. Experimental details

Antimony sulfide (Sb_2S_3) thin films were deposited by using the thermal evaporation technique, with a molybdenum boat serving as the source holder and fluorine-doped tin oxide (FTO)-coated glass substrates as the deposition surface. Before deposition, the substrates were subjected to ultrasonic cleaning in isopropyl alcohol for 10 minutes, followed by drying with nitrogen. The cleaned substrates and high-purity Sb_2S_3 powder (Thermo Fisher, 99.9%) were subsequently loaded into the thermal evaporation chamber.

The deposition process was carried out at an average pressure of 5×10^{-6} mbar, which was achieved using liquid nitrogen. The source-to-substrate distance was set to 16 cm, and the substrate temperature was maintained at 150 °C during deposition. A digital quartz crystal monitor was employed to monitor and control the deposition rate and film thickness. The deposition rate was maintained at 3.5–4 Å s^{-1} by adjusting the filament current to 85 A, resulting in a final Sb_2S_3 film thickness of 450 nm. Concurrently, silver (Ag) layers with thicknesses ranging from approximately 20 to 80 nm were deposited.

Post deposition, the films were sulfurized at 400 °C for 30 minutes in a vacuum of 900 mbar using a customized chemical vapor deposition (CVD) setup. Sulfur (100 mg, Thermo Fisher, 99.9998% purity) was evaporated in a single-zone furnace under a nitrogen atmosphere. After sulfurization, the films were cooled to room temperature under vacuum conditions, consistent with the procedure described in our previous study.[19] Table 1 presents the details of the deposited films.

3. Characterization

The structural properties of the silver-doped antimony sulfide (Sb_2S_3) films were analyzed by grazing incidence X-ray diffraction (GIXRD). Measurements were performed at room temperature with a Bruker AXS D8 Advance diffractometer, employing Cu Kα radiation over a 2θ angular range of 10–60° at a scanning rate of 0.1° min^{-1}.

The crystallite size was calculated using the Scherrer equation:

$$D = \frac{K\lambda}{\beta \cos\theta}$$

Table 1 Details of the silver-doped antimony sulfide thin films

Sample name	Thickness (nm) of silver (Ag) ± 5 nm
SA0	—
SA1	20
SA2	40
SA3	60
SA4	80

The microstrain and dislocation densities were calculated using the following equations:

$$\varepsilon = \frac{\beta}{4\tan\theta} \quad \text{and} \quad \delta = \frac{1}{D^2}$$

The interplanar spacing (d-spacing) was determined using Bragg's law:

$$d = \frac{\lambda}{2\sin\theta}$$

where D is the average crystallite size (in nm), β is the full-width at half maximum (FWHM) of the diffraction peak (in radians), K is a constant nearly equal to 0.9, λ is the wavelength of incident radiation approximately equal to 1.542 Å, θ is Bragg's angle (in radians), ε is the lattice strain, δ is the dislocation density, and d is the interplanar spacing.

Raman spectroscopy was conducted in a backscattering configuration using a Nd:YVO_4 diode-pumped solid-state laser with a 532 nm excitation wavelength. The surface morphology was examined using a scanning electron microscope (SEM) (Zeiss EVO MA18) operating at an acceleration voltage of 10 kV, whereas the elemental composition was analyzed *via* energy-dispersive X-ray spectroscopy (EDS) (Oxford INCA X-act). The surface topography was characterized *via* atomic force microscopy (AFM) in tapping mode using a Flex-Axiom AFM system. A wettability test was performed to determine the contact angle of the films. Optical absorption spectra were recorded using a UV-visible spectrophotometer (Shimadzu UV-1900) over a wavelength range of 190–1100 nm. Photoluminescence (PL) measurements were carried out with a fluorescence spectrometer using a Nd:YVO_4 diode-pumped solid-state laser with an excitation wavelength of 260 nm.

The photoelectrochemical (PEC) performance of the photoelectrodes was evaluated using a CompactStat.h potentiostat (IVIUM) in conjunction with a standard three-electrode PEC H-cell (Redox.me). The silver-doped antimony sulfide film served as the working electrode, a platinum (Pt) wire was used as the counter electrode, and an Ag/AgCl electrode functioned as the reference electrode. A 0.5 M Na_2SO_4 aqueous solution (pH = 7) was used as the electrolyte. The potential *versus* the reversible hydrogen electrode (RHE) was calculated using the appropriate conversion formula:

$$E_{\mathrm{RHE}} = E_{\mathrm{Ag/AgCl}} + E^{\circ}_{\mathrm{Ag/AgCl}} + 0.059 \times \mathrm{pH}$$

where $E^{\circ}_{\mathrm{Ag/AgCl}} = 0.197$ V *vs.* NHE at 28 °C.

The light source for the PEC experiments was a 1-Sun LED solar simulator (Redox.me), delivering a light intensity of 100 mW cm^{-2}. The films were illuminated in a backside illumination configuration, with an exposed area of 0.5 cm^2. Linear sweep voltammetry (LSV) and cyclic voltammetry (CV) measurements were conducted at a scan rate of 50 mV s^{-1}. Electrochemical impedance spectroscopy (EIS) was carried out over a frequency range of 0.1 Hz to 100 kHz using a sinusoidal voltage of 0.5 V.

4. Results and discussion

4.1. Structural analysis

The structures of all the samples confirm that antimony sulfide (Sb_2S_3) crystallizes in an orthorhombic structure, belonging to the *Pnma* space group (no. 62). This crystallographic configuration influences the material's preferred growth orientation and stacking behavior. In this study, the Pnma system is considered, wherein the infinite $(Sb_4S_6)_n$ chains extend along the [hk1] direction.[13]

Fig. 1 presents the grazing incidence X-ray diffraction (GIXRD) patterns of silver-doped Sb_2S_3 thin films, referenced against the standard JCPDS Card No. 42-1393.[20] The diffraction peak intensities corresponding to Sb_2S_3 phases exhibit variations across the samples, with the (hk0) planes generally showing greater intensity in the thin films compared to the (hkl) planes, indicating a preferential in-plane orientation. Notably, in sample SA4, the most intense peaks are observed at the (111), (021), and (221) planes, indicating a stronger perpendicular van der Waals interaction between the $(Sb_4S_6)n$ infinite ribbons, which preferentially grow along the [hk1] direction.[18]

For the silver-doped samples, the presence of the Ag_2S phase is confirmed by distinct peaks at 27.51°, 30.73°, and 45.60°, which correspond to the monoclinic $AgSbS_2$ phase (JCPDS No. 019-1137).[16] The presence of Ag_2S peaks was also confirmed, and no additional peaks associated with Sb_2O_3 (JCPDS No. 05-0534) were observed,[21] or metallic Ag was detected, confirming the absence of oxide impurities or unreacted silver. Furthermore, no significant shift in the diffraction peak was observed upon silver doping, suggesting that Ag incorporation does not induce substantial structural distortions in the Sb_2S_3 lattice.

Table 2 presents the crystallographic parameters obtained from the GIXRD patterns. The pristine SA0 sample exhibits a relatively small crystallite size. With increasing silver doping, the crystallite size progressively increases, reaching a maximum in the SA3 sample. Beyond this point, a reduction in crystallite size is observed. A similar trend is observed in the microstrain and dislocation density: both are initially high in the undoped SA0 sample, decrease with increasing silver concentration up to SA3, and then begin to increase again with further doping. This trend can be attributed to the role of silver doping in enhancing crystallite growth by reducing the number of lattice defects. This behavior suggests that moderate Ag incorporation enhances crystallinity by reducing structural defects and promoting grain growth. However, at higher doping levels (beyond SA3), excessive silver incorporation may introduce structural strain, further limiting crystallite growth. This effect is likely due to the solubility limit of Ag within the Sb_2S_3 lattice, potentially leading to phase segregation or the formation of secondary Ag-containing phases, which in turn degrade the overall crystal quality,[22] as indicated by the GIXRD patterns. The initial reduction in microstrain and dislocation density at lower silver concentrations suggests that silver atoms may occupy substitutional or interstitial sites, stabilizing the crystal structure.[17,23] Beyond a critical level of silver doping, strain can

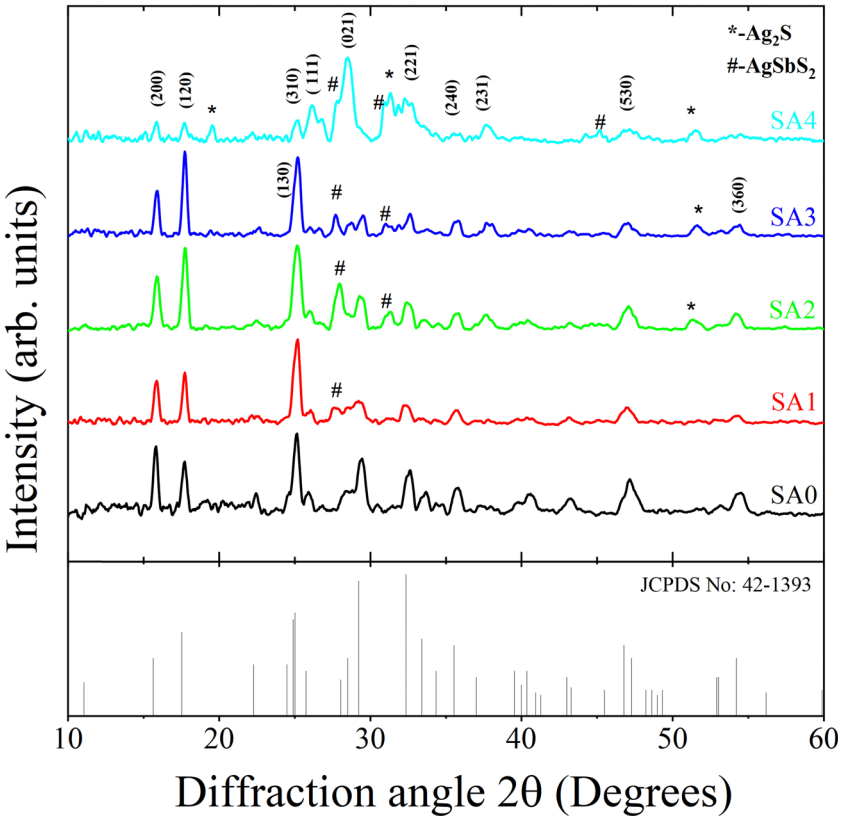

Fig. 1 GIXRD patterns of silver-doped antimony sulfide thin films.

result in lattice distortions and an increase in structural defects, thereby reducing the overall crystallinity.[24]

Fig. 2 presents the Raman spectra of silver (Ag)-doped antimony sulfide (Sb_2S_3) thin films, providing insights into their vibrational characteristics and structural modifications. The characteristic modes observed at 144, 192, 251, 280, and 322 cm^{-1} correspond to Sb_2S_3 vibrations, indicative of its stibnite phase. Specifically, the peaks at 280 and 322 cm^{-1} are attributed to antisymmetric and symmetric Sb–S stretching vibrations, respectively.[25] The modes at 144, 192, and 251 represent the antisymmetric bending vibrations of S–Sb–S and were attributed to symmetric bending vibrations of S–Sb–S.[26] The peak at 450 cm^{-1} is attributed to the FTO substrate.[27] The Raman modes at 144 and 192 cm^{-1} also suggest the presence of Ag_2S, with the 144 cm^{-1} peak corresponding to Ag lattice vibrations and the 192 cm^{-1} peak attributed to Ag–S stretching vibrations.[28] Furthermore, additional peaks at 491, 1246, and 1443 cm^{-1} are characteristic of Ag_2S.[29,30] An increase in the Ag concentration results in a corresponding increase in the intensity of these peaks, indicating increased incorporation of Ag into the Sb_2S_3 matrix. These Raman results further confirm the structural and crystallinity changes in the film, as they align well with the XRD measurements.

4.2. Morphological analysis

The effect of Ag incorporation on the surface morphology is demonstrated by scanning electron microscopy (SEM) images of silver-doped antimony sulfide (Sb_2S_3) thin films in Fig. 3. The undoped sample (SA0) has a porous grain structure, indicating irregular crystallization. With increasing Ag concentration, the grains become more compact and well-defined, as observed in samples SA1 and SA2, suggesting improved grain growth and enhanced crystallinity.[31]

At an intermediate doping level (sample SA3), the grain structure appears less compact, likely because the excessive Ag content alters nucleation and inhibits uniform grain growth. However, at a higher doping concentration (sample SA4), the compact morphology is restored, possibly due to dopant-

Table 2 Crystal parameters of silver-doped antimony sulfide films

Sample	Crystallite size (D in nm)	Microstrain (ε in 10^{-3})	Dislocation density (δ in $10^{15}/m^2$)	Interplanar distance (d_{hkl}) in Å
SA0	15.7	10.8	4.0	3.56
SA1	16.3	9.7	3.7	3.54
SA2	20.0	7.4	2.3	3.42
SA3	21.8	7.0	2.1	3.43
SA4	18.7	8.5	2.8	3.55

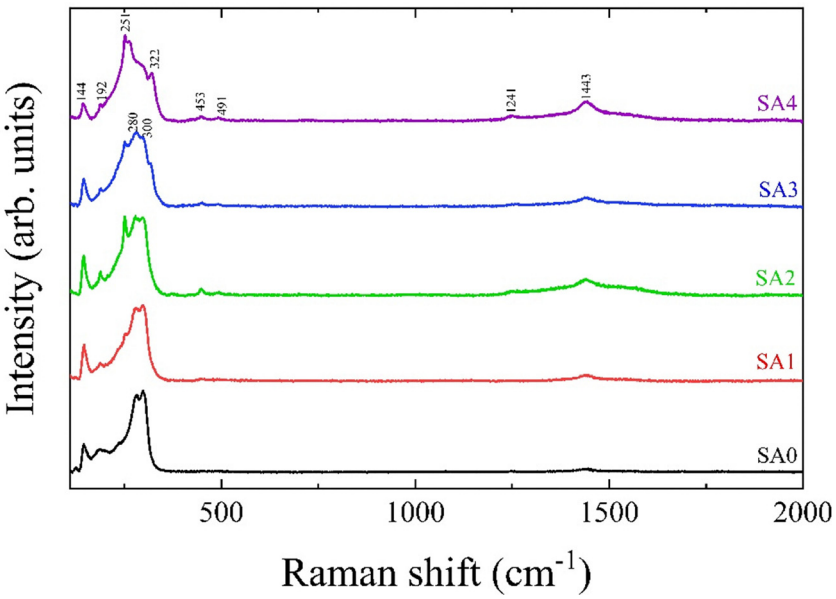

Fig. 2 Raman spectra of silver-doped antimony sulfide thin films.

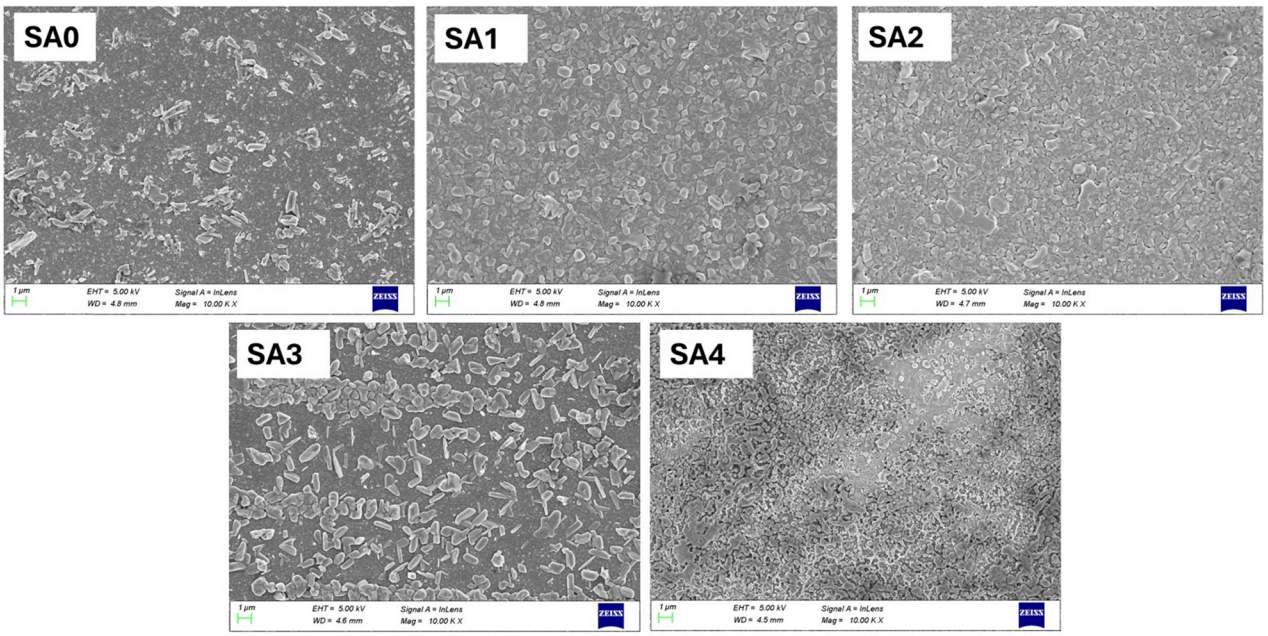

Fig. 3 SEM images of silver-doped antimony sulfide thin films.

induced recrystallization or the formation of secondary phases influencing the grain boundary energy.[32]

Atomic force microscopy (AFM) images in Fig. 4 show the surface morphology across the different samples. Changes in silver concentration correspond to fluctuations in surface roughness, as reflected in the roughness parameters: average roughness (R_a) and root mean square roughness (R_q), as shown in Table 3. The differences in roughness are likely linked to the morphological changes observed in Fig. 3. Compared with the silver-doped samples (SA1 to SA4), the undoped sample (SA0) has a rougher surface. Upon initial silver doping (sample SA1), the surface roughness decreases, likely due to enhanced film uniformity and improved crystallinity.[33] However, as the silver doping concentration increased (sample SA2), the development of larger agglomerates or the uneven distribution of silver atoms may have contributed to the surface roughness's subsequent growth. The surface roughness increased again, possibly due to the formation of larger agglomerates or the nonuniform distribution of silver atoms. In sample SA3, the roughness decreases as well, which may be attributed to an

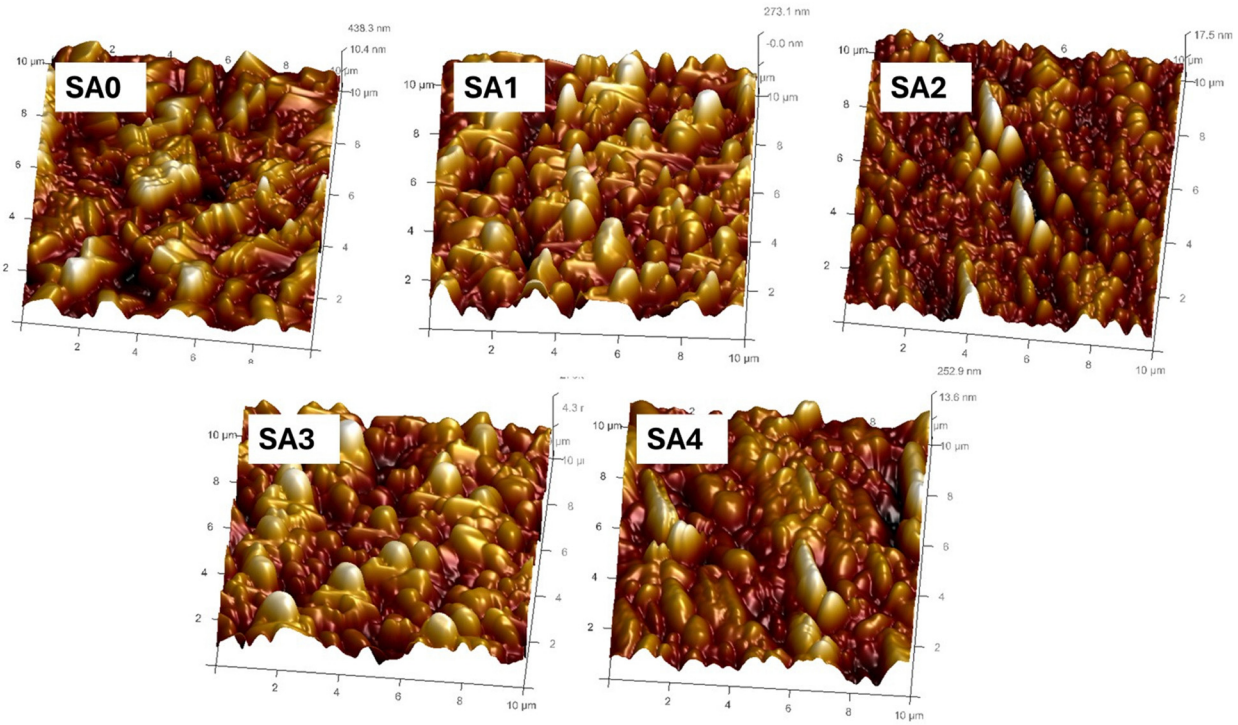

Fig. 4 AFM images of antimony sulfide films.

Table 3 Surface roughness parameters of antimony sulfide films

Sample name	R_q (nm)	R_a (nm)
SA0	121.0	96.1
SA1	78.4	61.9
SA2	81.9	65.2
SA3	55.0	36.5
SA4	62.3	48.0

optimal balance between silver incorporation and surface morphology. In the final sample (SA4), the roughness increases, possibly due to the oversaturation of silver, which leads to an increase in the number of grain boundaries and defects. These fluctuations in surface roughness are influenced by changes in silver content during deposition, which can alter molecular adhesion, nucleation rates, and growth dynamics on the substrate surface.[34]

4.3. Wettability test

The wettability of silver-doped antimony sulfide (Sb_2S_3) thin films was assessed through contact angle measurements, as shown in Fig. 5. The contact angle indicates the hydrophilic or hydrophobic nature of the samples. A contact angle greater than 90° suggests a hydrophobic surface, while an angle less than 90° indicates hydrophilicity. Hydrophilic surfaces tend to wet more easily with electrolyte, which can lead to reduced charge transfer resistance.[35] The results indicate that all the films exhibit hydrophobic behavior, with contact angles exceeding 90°. However, as the silver doping concentration increases, the contact angle progressively decreases, indicating a reduction in hydrophobicity.

Notably, sample SA3 has the lowest contact angle of 90°, suggesting a significant change in surface wettability at higher doping levels. This trend can be attributed to modifications in the surface energy and roughness induced by the incorporation of Ag. An increased Ag content likely alters the microstructure of the film, affecting the grain boundaries and surface texture, which in turn enhances water interactions.[36]

4.4. Compositional analysis

Energy-dispersive spectroscopy (EDS) was used to analyze the elemental composition of silver-doped antimony sulfide thin films. Table 4 presents the atomic percentage compositions, illustrating the impact of Ag doping on the relative concentrations of antimony (Sb) and sulfur (S). These results specify that as the Ag concentration increases, the sulfur content progressively decreases, whereas the antimony content remains relatively unchanged. This trend suggests that Ag atoms may preferentially substitute for sulfur sites within the Sb_2S_3 crystal lattice. This substitution leads to a reduction in the number of sulfur atoms without significantly altering the Sb concentration, which may modify the electronic and structural properties of the material. The observed elemental variations provide insight into the dopant-induced compositional changes.

Fig. 6(a) presents the X-ray photoelectron spectroscopy (XPS) survey and core-level spectra of silver-doped antimony sulfide thin films, providing insights into their surface chemical composition. The binding energy peaks were deconvoluted using a Gaussian–Lorentzian function, and all the spectra were

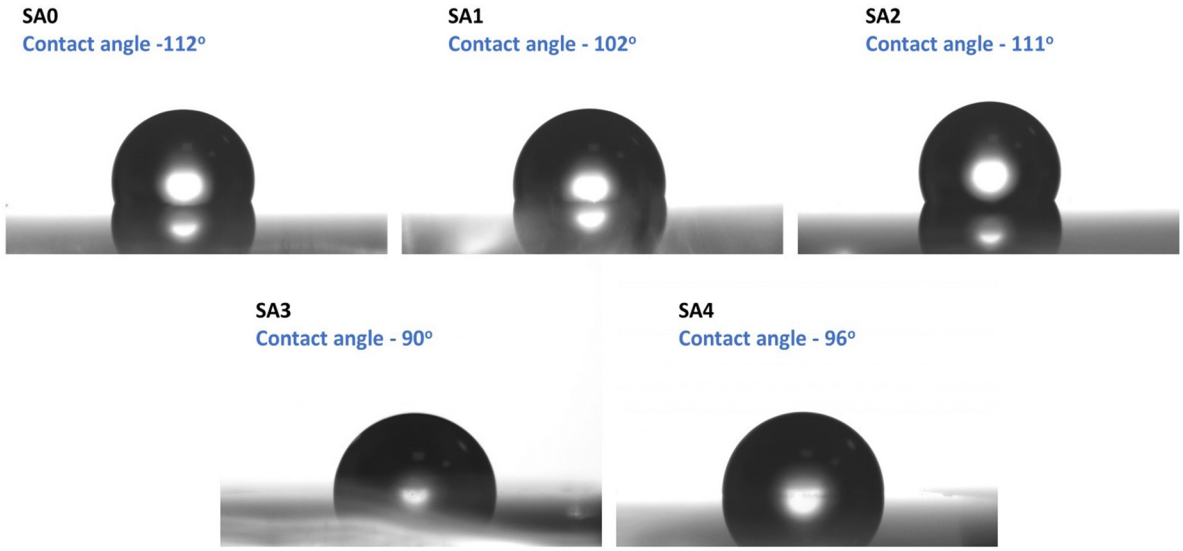

Fig. 5 Contact angle of silver-doped antimony sulfide thin films.

calibrated by referencing the C 1s peak at 284.6 eV. The survey spectrum confirms the presence of Sb, S, and Ag from the sample, whereas the C and O signals originate from adventitious carbon and surface-absorbed oxygen.

The Ag 3d core-level spectrum displays distinct doublets at 373.8 eV (Ag $3d_{3/2}$) and 367.8 eV (Ag $3d_{5/2}$), with a spin-orbital splitting energy of 6.0 eV, confirming the presence of Ag^{+} species. The sharp nature of these peaks suggests that Ag has not undergone oxidation, indicating that it exists in either a metallic state or as Ag–S bonds.[37,38]

The Sb 3d core-level spectrum exhibited clear doublets at binding energies of 539.0 eV and 529.6 eV, corresponding to the Sb $3d_{3/2}$ and Sb $3d_{5/2}$ components of Sb_2S_3, respectively, with a spin–orbit splitting energy of 9.4 eV. The area ratio of the $3d_{5/2}$ peak to the $3d_{3/2}$ peak is approximately 1.5 (3 : 2), aligning with the expected ratio.[39–41] Furthermore, weak peaks observed at binding energies of 540.0 eV and 530.4 eV can be attributed to Sb_2O_3.[42] Notably, in the pristine sample (SA0), no oxide-related peaks of antimony are detected, indicating the absence of Sb_2O_3. With increasing silver (Ag) doping concentration, the intensity of these oxide peaks becomes progressively more pronounced, especially in samples SA3 and SA4, indicating a higher degree of Sb_2O_3 formation at elevated doping levels. A plausible explanation is that after Ag deposition on Sb_2S_3, surface oxidation occurred, leading to the formation of Ag_2O. During the subsequent sulfurization process, conducted at 400 °C for 30 minutes, the surface Ag_2O may have thermally decomposed into metallic Ag and oxygen.[43,44] The released oxygen could have reacted with antimony at the surface, resulting in the formation of Sb_2O_3 during the sulfurization. Additionally, the O 1s peak observed near 532 eV supports the presence of oxygen species. However, the overlap in binding energies between antimony and oxygen in this region makes it difficult to accurately distinguish and resolve the individual contributions.[45,46]

The S 2p core-level spectrum reveals doublets at 160.8 eV and 161.9 eV, corresponding to the S $2p_{3/2}$ and S $2p_{1/2}$ components of sulfur (S). The area under the curve ratio of $2p_{3/2}$ to $2p_{1/2}$ is 2 : 1, with an energy separation of 1.1 eV, indicating the S^{2-} oxidation state.[47,48] Additionally, the peaks at 163.0 eV and 164.0 eV correspond to sulfur species associated with oxidation, such as sulfur oxides and sulfates.[49] As Ag doping increases, the intensity of these oxidation-related peaks decreases, further suggesting that Ag incorporation increases surface oxidation. According to both core spectra, a higher binding energy generally correlates with higher oxidation states of the material.[47]

XPS analysis confirmed the presence of oxide species on the sample surface, particularly for Sb 3d and S 2p, which was likely due to ambient oxidation. However, this surface oxidation is not reflected in the bulk phase characterization, as corroborated by X-ray diffraction (XRD) and Raman spectroscopy, which show no evidence of oxide formation. Furthermore, the incorporation of Ag into the Sb_2S_3 matrix was validated by the observed phase formation of Ag_2S, confirming successful doping.

Table 4 Atomic percentages of silver-doped antimony sulfide thin films

Sample name	Atomic percentage (%)		
	Antimony (Sb)	Sulfur (S)	Silver (Ag)
SA0	32	68	0
SA1	33	65	2
SA2	32	63	5
SA3	32	60	8
SA4	30	58	12

4.5. Optical analysis

Fig. 7 presents the optical characterization of silver-doped antimony sulfide (Sb_2S_3) thin films, including (a) absorbance spectra, (b) absorption coefficient spectra, (c) Tauc plots, and (d) photoluminescence (PL) spectra. The variation in the silver

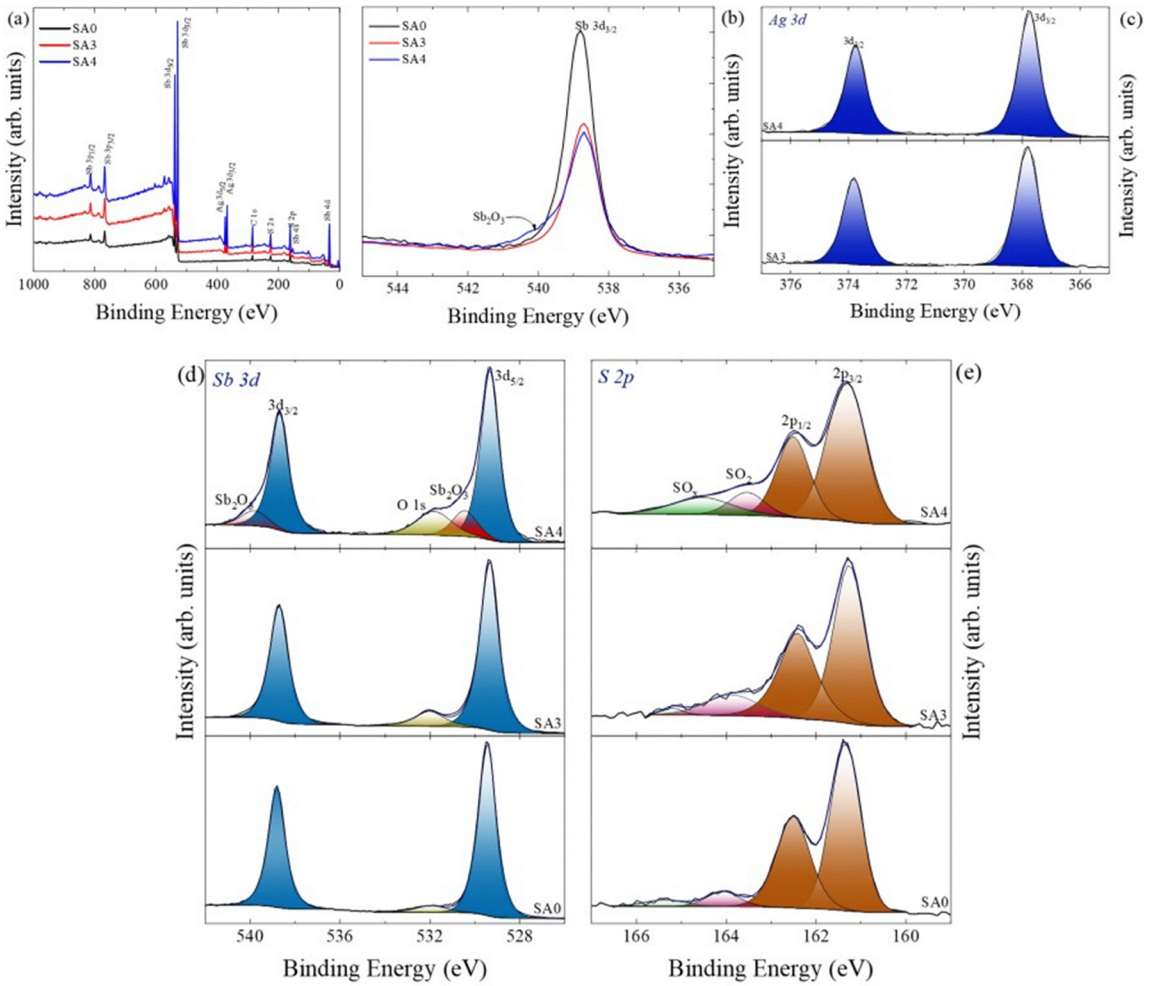

Fig. 6 (a) and (b) XPS survey spectra, (c)–(e) core spectra of Ag 3d, Sb 3d, and S 2p of the silver-doped antimony sulfide film.

doping concentration significantly influences the optical properties, particularly the film absorbance, absorption coefficient, and optical band gap.

The absorbances and absorption coefficients of the Sb_2S_3 thin films remain relatively stable up to sample SA2, beyond which a noticeable decline is observed. This reduction can be attributed to the increased incorporation of Ag, which alters the material's electronic structure and optical transitions. At lower doping concentrations (up to SA2), Ag atoms likely integrate into the Sb_2S_3 lattice without causing significant disruptions to the electronic band structure, thereby maintaining a stable absorption profile.[50,51] However, at higher doping levels (SA3 and SA4), excessive Ag incorporation may introduce structural defects, modify the carrier concentration, and promote the formation of secondary phases such as Ag_2S. These changes can reduce the density of optically active states, thereby decreasing the overall absorbance and absorption coefficient. Furthermore, increased Ag content may influence crystallinity and surface roughness, contributing to enhanced light scattering losses and further diminishing optical absorption.[52]

The change in absorbance and absorption coefficient is closely related to the variation in the optical band gap, as calculated using the Tauc plots. As shown in Table 5, the undoped sample (SA0) has a band gap of around 1.79 eV. With the introduction of Ag dopant, the band gap reduces to 1.66 eV for sample SA1. After this, a gradual increase in band gap is observed, reaching around 1.75 eV for samples SA3 and SA4.[53–55] The initial decrease in band gap can be explained by the formation of localized energy states within the band structure due to the substitution of Ag in the Sb_2S_3 lattice. These states lead to band tailing, which narrows the effective band gap.[56,57] At higher doping levels, the increase in band gap may result from the Burstein–Moss effect. This effect occurs when increased carrier concentration shifts the conduction band and valence band edges, leading to a widening of the band gap.[58] In addition, higher Ag doping may introduce more crystal defects, structural changes, and secondary phases. These changes can influence carrier mobility and transition probability, which also affect the band gap. Variations in crystallinity, grain boundaries, and surface texture at higher doping levels may cause increased light scattering and reduced absorption, further impacting the optical properties of the films.[53,59]

The photoluminescence (PL) spectra of silver-doped antimony sulfide thin films, shown in Fig. 7(d), display emission

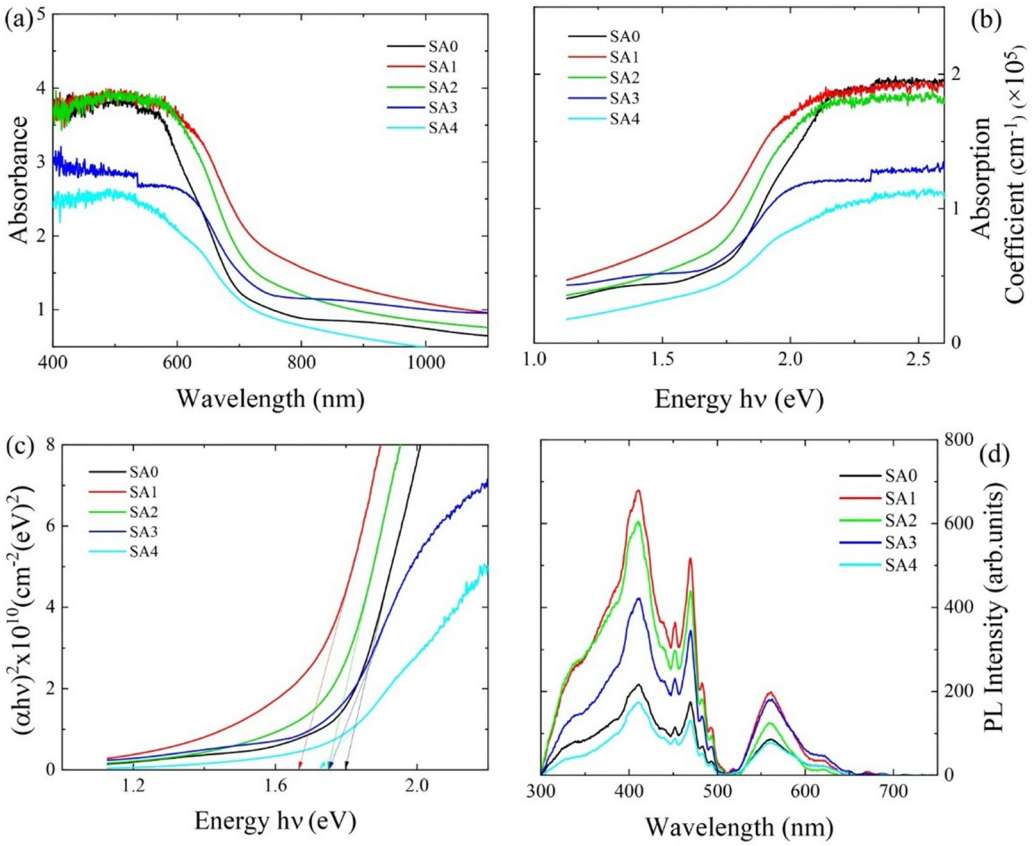

Fig. 7 (a) Absorbance spectra, (b) absorption coefficient spectra, (c) Tauc plots, and (d) photoluminescence spectra of silver-doped antimony sulfide films.

Table 5 Band gap values of silver-doped antimony sulfide thin films

Sample name	Band gap (eV) ± 0.02 eV
SA0	1.79
SA1	1.66
SA2	1.75
SA3	1.75
SA4	1.72

peaks at 410, 440, 498, 550, and 630 nm. The emissions at 410, 440, and 498 nm correspond to blue emission, which is likely caused by defects and trap states.[60,61] The green emission at 550 nm is thought to arise from sulfur depletion or surface defects.[62] The 630 nm emission is attributed to the band-edge luminescence of Sb_2S_3.[63] The PL intensity is observed to be lowest for the undoped sample (SA0). Upon doping (SA1), the emission intensity increases, but with further doping, it begins to decrease. The initial increase in the PL intensity can be explained by the enhanced recombination of charge carriers, as the introduction of dopants creates energy levels that promote radiative recombination. However, as the doping concentration continues to increase, nonradiative recombination pathways, such as those associated with defects or impurities, become more dominant. These defects trap carriers, reducing the number of electrons and holes available for radiative recombination, which leads to a decrease in the PL emission intensity.[64] Hence, excessive doping eventually suppresses PL emission due to increased nonradiative losses.

4.6. Electrochemical analysis

Fig. 8(a) presents the Nyquist plots obtained from electrochemical impedance spectroscopy (EIS) under dark conditions. The semicircle radius in these plots represents the charge transfer resistance at the semiconductor–electrolyte interface, as well as the total resistance of the electrode. For the pristine sample, a smaller semicircle radius is observed, indicating a lower charge transfer resistance.[65,66] Upon doping, the radius initially increases, suggesting an increase in resistance, but beyond a certain point, it decreases again. The lower charge transfer resistance of the pristine sample can be attributed to its porous morphology, as observed in the SEM images, along with its high absorbance and absorption coefficient, low photoluminescence (PL) emission intensity, and increased surface roughness. These factors collectively enhance charge transport and reduce interfacial resistance.[48]

Fig. 8(b) and (c) present the cyclic voltammetry (CV) and linear sweep voltammetry (LSV) curves of silver-doped antimony sulfide thin films. The onset potential and current density are key indicators of photoelectrochemical (PEC)

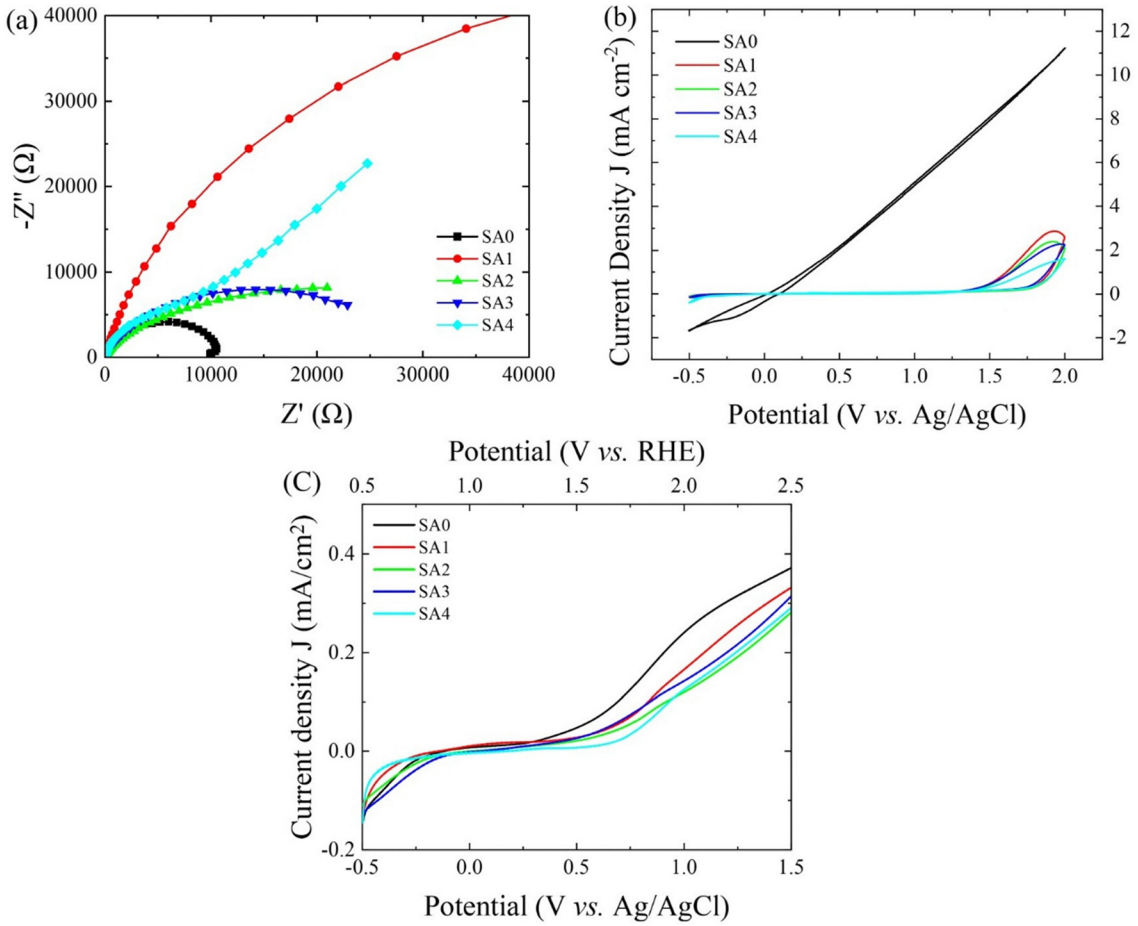

Fig. 8 (a) Nyquist plots, (b) cyclic voltammograms, and (c) LSV curves of silver-doped antimony sulfide films.

performance, where a lower onset potential and higher current density signify enhanced water-splitting efficiency.

The pristine antimony sulfide sample exhibited the highest current density, reaching 11.87 mA cm^{-2} in the CV curve and 0.38 mA cm^{-2} in the LSV curve. However, after silver doping, a noticeable decrease in the current density is observed. In the CV curve, the current density decreases to 3 mA cm^{-2}, while in the LSV curve, it drops to a minimum of 0.29 mA cm^{-2}. The decrease in photoelectrochemical performance after silver doping is mainly due to changes in band gap, surface morphology, and chemical composition. Doping with silver modifies the surface morphology and roughness, as seen in morphological studies. These changes affect the distribution of electrochemically active sites. A smoother surface may reduce the number of reactive sites, which can lower charge transfer efficiency. The undoped sample had a band gap of 1.79 eV. With initial silver doping, the band gap decreased to 1.66 eV. This reduction allowed better absorption of visible light and led to the generation of more charge carriers. However, with a further increase in silver concentration, the band gap increased again to about 1.75 eV. This increase is likely due to the Burstein–Moss effect, where a higher carrier concentration shifts the Fermi level and increases the energy required for electronic transitions. A wider band gap reduces light absorption and limits the generation of charge carriers.[24,67,68] Another contributing factor to the reduction in current density may be the formation of Sb_2O_3, as evidenced by the appearance of oxide-related peaks in the XPS spectra of doped samples. The presence of Sb_2O_3 can introduce insulating domains or surface states that trap carriers, further impeding efficient charge transport and contributing to the overall decline in sample performance.[69] Additionally, an increase in the contact angle indicates a decrease in wettability, which can impede electrolyte penetration and hinder charge transfer at the electrode–electrolyte interface.[70] The photoluminescence (PL) spectra reveal enhanced emission intensity and variations in absorbance after doping, suggesting that alterations in defect states and recombination dynamics could negatively affect charge carrier transport.[71]

5. Conclusions

Silver-doped antimony sulfide (Sb_2S_3) thin films were successfully fabricated on FTO substrates *via* thermal evaporation and chemical vapor deposition techniques. Structural analysis *via* GIXRD revealed a shift in the preferred orientation from the (*hk*0) to (*hk*1) plane after doping. SEM and AFM analyses demonstrated a morphological transition from a porous to a

denser structure, accompanied by a reduction in surface roughness from 96.1 nm to 59.6 nm. Optical analysis revealed a consistent bandgap of ~1.7 eV across all the samples, with the pristine film exhibiting the highest absorbance. Electrochemical characterization *via* CV and LSV demonstrated that the pristine Sb_2S_3 film achieved the highest current density (11.87 mA cm^{-2} and 0.38 mA cm^{-2}, respectively), whereas doping led to a noticeable decrease, which was attributed to a reduced electroactive surface area and hindered electrolyte interaction due to increased hydrophobicity. The enhanced PL emission intensity in the doped films suggests changes in the defect state and increased carrier recombination, further impacting the charge transport and PEC performance. Overall, silver doping significantly alters the physicochemical properties of Sb_2S_3 thin films, and while it improves surface compactness, it adversely affects the photoelectrochemical water-splitting efficiency, emphasizing the need for balanced surface modification strategies.

Conflicts of interest

There are no conflicts of interest to declare.

Data availability

Most data pertaining to this article are provided within the article itself. Any missing data can be provided on a reasonable request to the corresponding author.

Acknowledgements

The authors express their gratitude to Dr (Prof.) Ajay Kumar Kushwaha, Department of Metallurgical Engineering & Materials Science (MEMS), Indian Institute of Technology Indore, for providing the electrochemical measurements. Special thanks are extended to Dr V. Raghavendra Reddy and Mr Anil Gome from the UGC-DAE Consortium, Indore, for their assistance with GIXRD measurements, and Manipal Academy of Higher Education for providing financial support through the Dr TMA Pai PhD scholarship. Dr Sudha D. Kamath (MIT Manipal) is acknowledged for photoluminescence measurements. Mr Pramod R. Nadig and Ms B. S. Srujana (Manipal Institute of Technology, Manipal) are recognized for their assistance with the analysis.

References

1 A. Darga, *et al.*, On charge carrier recombination in Sb_2S_3 and its implication for the performance of solar cells, *J. Phys. Chem. C*, 2013, **117**(40), 20525–20530, DOI: **10.1021/jp4072394**.

2 H. Lei, J. Chen, Z. Tan and G. Fang, Review of Recent Progress in Antimony Chalcogenide-Based Solar Cells: Materials and Devices, *Sol. RRL*, 2019, **3**(6), 1–27, DOI: **10.1002/solr.201900026**.

3 D. M. Kavya, Y. N. Sudhakar, A. Timoumi and Y. Raviprakash, Thickness-dependent performance of antimony sulfide thin films as a photoanode for enhanced photoelectrochemical water splitting, *RSC Adv.*, 2025, **15**(17), 13691–13702, DOI: **10.1039/d5ra00586h**.

4 S. De, R. Bhar, A. Pangas, S. Mondal, B. K. Dubey and S. Maity, Resource efficient metal extraction and silicon wafer recovery from end-of-life monocrystalline solar cells: A chemical and environmental perspective, *Waste Manage.*, 2025, **203**, 114867, DOI: **10.1016/j.wasman.2025.114867**.

5 S. Manna, *et al.*, Antireflection cum photocatalytic with superhydrophilic based durable single layer mesoporous TiO_2 - ZrO_2 coating surface for efficient solar photovoltaic application, *Sustainable Energy Technol. Assessments*, 2023, **57**, 103236, DOI: **10.1016/j.seta.2023.103236**.

6 Y. C. Wang, *et al.*, A Stable and Efficient Photocathode Using an Sb_2S_3 Absorber in a Near-Neutral Electrolyte for Water Splitting, *ACS Appl. Energy Mater.*, 2020, **3**(7), 6188–6194, DOI: **10.1021/acsaem.0c00210**.

7 A. Apolinário, T. Lopes, C. Costa, J. P. Araújo and A. M. Mendes, Multilayered WO_3 Nanoplatelets for Efficient Photoelectrochemical Water Splitting: The Role of the Annealing Ramp, *ACS Appl. Energy Mater.*, 2019, **2**(2), 1040–1050, DOI: **10.1021/acsaem.8b01530**.

8 H. Lei, *et al.*, Copper doping of Sb_2S_3: fabrication, properties, and photovoltaic application, *J. Mater. Sci. Mater. Electron.*, 2019, **30**(24), 21106–21116, DOI: **10.1007/s10854-019-02481-9**.

9 U. S. Ele, I. C. Nworie, A. O. Ojobeagu, P. B. Otah and E. N. Nwulegu, Influence of Magnesium Doping Concentrations and annealing on the Transmittance and Energy Band-gap of Sb_2S_3 Thin Films Deposited via Chemical Bath Deposition Technique, *Niger. J. Phys*, 2024, **33**(1), 23–27, DOI: **10.62292/njp.v33i1.2024.185**.

10 R. Tang, *et al.*, N-Type Doping of Sb_2S_3 Light-Harvesting Films Enabling High-Efficiency Planar Heterojunction Solar Cells, *ACS Appl. Mater. Interfaces*, 2018, **10**(36), 30314–30321, DOI: **10.1021/acsami.8b08965**.

11 Z. Cai, C. M. Dai and S. Chen, Intrinsic Defect Limit to the Electrical Conductivity and a Two-Step p-Type Doping Strategy for Overcoming the Efficiency Bottleneck of Sb2S3-Based Solar Cells, *Sol. RRL*, 2020, **4**(4), 1900503, DOI: **10.1002/solr.201900503**.

12 P. Myagmarsereejid, M. Ingram, M. Batmunkh and Y. L. Zhong, Doping Strategies in Sb_2S_3 Thin Films for Solar Cells, *Small*, 2021, **17**(39), 1–17, DOI: **10.1002/smll.202100241**.

13 A. Chihi, Effect of Ruthenium doping in tailoring structure, optical and electrical properties of Sb_2S_3 thin film synthesized via electrodeposition technique, *J. Mater. Sci. Mater. Electron.*, 2023, **34**(31), 1–18, DOI: **10.1007/s10854-023-11516-1**.

14 S. Mushtaq, B. Ismail, M. Aurang Zeb, N. J. Suthan Kissinger and A. Zeb, Low-temperature synthesis and characterization of Sn-doped Sb_2S_3 thin film for solar cell applications, *J. Alloys Compd.*, 2015, **632**, 723–728, DOI: **10.1016/j.jallcom.2015.01.307**.

15 M. Ishaq, *et al.*, Efficient Copper-Doped Antimony Sulfide Thin-Film Solar Cells via Coevaporation Method, *Solar RRL*, 2019, **3**(12), 1900305, DOI: **10.1002/solr.201900305**.

16 C. Lebastard, C. L. Hassam, T. Suzuki, T. Uchikoshi, Y. Thimont and D. Berthebaud, Investigation of Silver and Copper Doping on Antimony Sulfide Thin Films Obtained by Electrophoretic Deposition, *J. Phys. Chem. C*, 2024, **128**(42), 18093–18101, DOI: **10.1021/acs.jpcc.4c04781**.

17 C. J. Diliegros-Godines, J. Santos Cruz, N. R. Mathews and M. Pal, Effect of Ag doping on structural, optical and electrical properties of antimony sulfide thin films, *J. Mater. Sci.*, 2018, **53**(16), 11562–11573, DOI: **10.1007/s10853-018-2420-3**.

18 M. Yang, *et al.*, Tailoring the Crystallographic Orientation of a Sb_2S_3Thin Film for Efficient Photoelectrochemical Water Reduction, *ACS Catal.*, 2022, **12**(14), 8175–8184, DOI: **10.1021/acscatal.2c01384**.

19 D. M. Kavya, *et al.*, Two-step synthesis of antimony sulfide thin films: enhancement in physical properties through sulfurization, *Mater. Res. Express*, 2024, **11**(4), 46402, DOI: **10.1088/2053-1591/ad3897**.

20 A. Chihi, Gamma-irradiated stibnite thin films set a remarkable benchmark performance for photoelectrochemical water splitting, *RSC Adv.*, 2024, **14**(18), 12475–12495, DOI: **10.1039/d4ra01382d**.

21 Y. Peng, *et al.*, Preparation of Sb_2O_3/Sb_2S_3/FeOOH composite photoanodes for enhanced photoelectrochemical water oxidation, *Trans. Nonferrous Met. Soc. China*, 2020, **30**(6), 1625–1634, DOI: **10.1016/S1003-6326(20)65325-0**.

22 A. Maiti and S. K. Srivastava, N, Ru Codoped Pellet Drum Bundle-Like Sb_2S_3: An Efficient Hydrogen Evolution Reaction and Hydrogen Oxidation Reaction Electrocatalyst in Alkaline Medium, *ACS Appl. Mater. Interfaces*, 2020, **12**(6), 7057–7070, DOI: **10.1021/acsami.9b17368**.

23 W. Dong, *et al.*, Enhanced Sb_2S_3 crystallisation by electric field induced silver doping, *Thin Solid Films*, 2016, **616**, 80–85, DOI: **10.1016/j.tsf.2016.07.068**.

24 Z. Wang, L. Li, L. Hong, X. Shi, Y. Lu and J. Su, Bi Doped Sb_2S_3 Thin Film Synthesized by a Two-Step Approach with Enhanced Photoelectrochemical Water Splitting Performance, *J. Electrochem. Soc.*, 2022, **169**(6), 066508, DOI: **10.1149/1945-7111/ac6447**.

25 S. Yuan, *et al.*, Postsurface Selenization for High Performance Sb_2S_3 Planar Thin Film Solar Cells, *ACS Photonics*, 2017, **4**(11), 2862–2870, DOI: **10.1021/acsphotonics.7b00858**.

26 M. Medles, *et al.*, Raman and optical studies of spray pyrolysed Sb_2S_3 thin films, *J. Optoelectron. Adv. Mater.*, 2014, **16**(5–6), 726–731.

27 C. Y. Kim and D. H. Riu, Raman scattering, electrical and optical properties of fluorine-doped tin oxide thin films with (200) and (301) preferred orientation, *Mater. Chem. Phys.*, 2014, **148**(3), 810–817, DOI: **10.1016/j.matchemphys.2014.08.055**.

28 I. Martina, R. Wiesinger and M. Schreiner, Micro-Raman Characterisation of Silver Corrosion Products: Instrumental Set Up and Reference, *e-Preservation Sci.*, 2012, **9**, 1–8.

29 M. H. Azarian, S. Nijpanich, N. Chanlek and W. Sutapun, Probing capping mechanisms and polymer matrix loading of biogenic vaterite $CaCO_3$-Ag hybrid through X-ray photoelectron spectroscopy (XPS), *RSC Adv.*, 2024, **14**(21), 14624–14639, DOI: **10.1039/d4ra01710b**.

30 Y. Delgado-Beleño, *et al.*, Breathing Raman modes in Ag_2S nanoparticles obtained from F9 zeolite matrix, *Chem. Phys.*, 2015, **463**, 106–110, DOI: **10.1016/j.chemphys.2015.10.009**.

31 U. Chalapathi, B. Poornaprakash, C. H. Ahn and S. H. Park, Large-grained Sb_2S_3 thin films with Sn-doping by chemical bath deposition for planar heterojunction solar cells, *Mater. Sci. Semicond. Process.*, 2018, **84**, 138–143, DOI: **10.1016/j.mssp.2018.05.017**.

32 S. Salinas-Beltrán, J. R. Gaitán-Arevalo and L. A. González, Improvement of the photoelectrical properties of chemical bath-deposited Sb_2S_3 thin films with low copper doping, *J. Mater. Sci. Mater. Electron.*, 2024, **35**(7), 1–13, DOI: **10.1007/s10854-024-12256-6**.

33 S. Bhat, K. M. Sandeep, P. Kumar, M. P. Venu, S. M. Dharmaprakash and J. S. Bhat, Effect of Al doping on the carrier transport characteristics of TiO_2 thin films anchored on glass substrates, *Appl. Phys. A Mater. Sci. Process*, 2019, **125**(3), 1–11, DOI: **10.1007/s00339-019-2464-5**.

34 F. Bensouici, *et al.*, Al doping effect on the morphological, structural and photocatalytic properties of TiO_2 thin layers, *Thin Solid Films*, 2016, **616**, 655–661, DOI: **10.1016/j.tsf.2016.09.046**.

35 S. K. Shinde, D. P. Dubal, G. S. Ghodake and V. J. Fulari, Electronic impurities (Fe, Mn) doping in CdSe nanostructures for improvements in photoelectrochemical applications, *RSC Adv.*, 2014, **4**(63), 33184–33189, DOI: **10.1039/c4ra02791d**.

36 D. D. Purkayastha, R. Brahma, M. G. Krishna and V. Madhurima, Effects of metal doping on photoinduced hydrophilicity of SnO_2 thin films, *Bull. Mater. Sci.*, 2015, **38**(1), 203–208, DOI: **10.1007/s12034-014-0820-9**.

37 Z. Zhang, *et al.*, Ultrafast and broadband photodetection based on selenized $AgSbS_2$ thin films prepared by spray pyrolysis deposition and modified with indium nitrate, *J. Mater. Chem. A*, 2024, **14**, 4739–4751, DOI: **10.1039/d3ta06426c**.

38 X. Liu, *et al.*, Improving the optoelectronic properties of single-crystalline antimony sulfide rods through simultaneous defect suppression and surface cleaning, *J. Mater. Chem. A*, 2023, **11**(16), 8826–8835, DOI: **10.1039/d3ta00954h**.

39 J. Han, *et al.*, Solution-Processed Sb2S3 Planar Thin Film Solar Cells with a Conversion Efficiency of 6.9% at an Open Circuit Voltage of 0.7 V Achieved via Surface Passivation by a SbCl3 Interface Layer, *ACS Appl. Mater. Interfaces*, 2020, **12**(4), 4970–4979, DOI: **10.1021/acsami.9b15148**.

40 D. H. Kim, *et al.*, Highly reproducible planar Sb_2S_3-sensitized solar cells based on atomic layer deposition, *Nanoscale*, 2014, **6**(23), 14549–14554, DOI: **10.1039/c4nr04148h**.

41 L. Zhang, *et al.*, Sequential deposition route to efficient Sb_2S_3 solar cells, *J. Mater. Chem. A*, 2018, **6**(43), 21320–21326, DOI: **10.1039/c8ta08296k**.

42 Y. C. Choi, D. U. Lee, J. H. Noh, E. K. Kim and S. Il Seok, Highly improved Sb_2S_3 sensitized-inorganic-organic heterojunction solar cells and quantification of traps by deep-level transient spectroscopy, *Adv. Funct. Mater.*, 2014, **24**(23), 3587–3592, DOI: 10.1002/adfm.201304238.

43 E. S. B. V, RKCL3143 Oxygen states during thermal decomposition of ag20: xps and ups study A. L. Boronin, S. V. Koseheev, O. V. Kalinkina and G. M. Zhidomirov, *Science*, 1998, **63**(2), 291–296.

44 A. Ananth and Y. S. Mok, Dielectric barrier discharge (DBD) plasma assisted synthesis of Ag_2O nanomaterials and Ag_2O/RuO_2 nanocomposites, *Nanomaterials*, 2016, **6**(3), 42, DOI: 10.3390/nano6030042.

45 X. Liu, *et al.*, Grain Engineering of Sb_2S_3 Thin Films to Enable Efficient Planar Solar Cells with High Open-Circuit Voltage, *Adv. Mater.*, 2024, **36**(1), 2305841, DOI: 10.1002/adma.202305841.

46 M. Liu, Y. Gong, Z. Li, M. Dou and F. Wang, A green and facile hydrothermal approach for the synthesis of high-quality semi-conducting Sb_2S_3 thin films, *Appl. Surf. Sci.*, 2016, **387**, 790–795, DOI: 10.1016/j.apsusc.2016.06.126.

47 A. Shaheen, J. M. Sturm, R. Ricciardi, J. Huskens, C. J. Lee and F. Bijkerk, Characterization of Self-Assembled Monolayers on a Ruthenium Surface, *Langmuir*, 2017, **33**(25), 6419–6426, DOI: 10.1021/acs.langmuir.7b01068.

48 A. Maiti, S. Chatterjee and A. J. Pal, Sulfur-Vacancy Passivation in Solution-Processed Sb_2S_3 Thin Films: Influence on Photovoltaic Interfaces, *ACS Appl. Energy Mater.*, 2020, **3**(1), 810–821, DOI: 10.1021/acsaem.9b01951.

49 Y. Zhou, J. Si, H. Wang, X. Li, S. Zhang and C. Deng, Co_9S_8@NiFe-LDH Bifunctional Electrocatalysts as High-Efficiency Cathodes for Zn-Air Batteries, *Energy Fuels*, 2023, **37**(13), 9619–9625, DOI: 10.1021/acs.energyfuels.3c00938.

50 S. H. Zyoud and A. F. Omar, Investigating the role of Ag-doped ZnO thin films in UV photodetectors produced via laser assisted chemical bath growth technique, *Phys. B: Condens. Matter.*, 2024, **694**, 416406, DOI: 10.1016/j.physb.2024.416406.

51 M. Prabhu, M. Marikkannan, M. S. Pandian, P. Ramasamy and K. Ramachandran, Effect of zinc and indium doping in chalcogenide (CdS/Te) nanocomposites towards dye-sensitized solar cell applications, *J. Phys. Chem. Solids*, 2022, **168**, 110802, DOI: 10.1016/j.jpcs.2022.110802.

52 Y. T. Song, *et al.*, Novel TiO_2/Sb_2S_3 heterojunction with whole visible-light response for photoelectrochemical water splitting reactions, *RSC Adv.*, 2016, **6**(54), 49130–49137, DOI: 10.1039/c6ra04094b.

53 S. M. Salim, M. B. Seddek and A. M. Salem, and Islam, Low-temperature synthesis of Ag-doped Sb_2S_3 thin films and its characterization, *J. Appl. Sci. Res.*, 2010, **6**(9), 1352–1358.

54 E. Gnenna, N. Khemiri, M. I. Alonso and M. Kanzari, Optical characterization of Sb2S3 vacuum annealed films by UV–VIS–NIR spectroscopy and spectroscopic ellipsometry: Determining the refractive index and the optical constants, *Optik (Stuttg)*, 2022, **268**, 169740, DOI: 10.1016/j.ijleo.2022.169740.

55 H. Li, H. Tang, J. Yu, J. Cheng and L. Li, Strategy of stacking double absorbers to gain high efficiency in silver antimony sulfide selenide-based thin film solar cell, *J. Mater. Chem. C*, 2024, **12**(9), 3063–3071, DOI: 10.1039/d3tc03794k.

56 P. C. Kumar, *et al.*, Tuning Hydrophilicity and Photoresponse by Interfacial Ag Diffusion in the Sb_2S_3 Layer for Optoelectronic Applications: An Experimental and Computational Study, *J. Phys. Chem. C*, 2024, **128**(39), 16740–16753, DOI: 10.1021/acs.jpcc.4c04263.

57 N. Jessy Mathew, R. Oommen, P. Usha Rajalakshmi and C. Sanjeeviraja, Investigations on the Se-doped Sb_2S_3 thin films, *Chalcogenide Lett.*, 2011, **8**(7), 41–446.

58 A. Tubtimtae, P. Pluengphon and B. Inceesungvorn, Indium dopant-induced morphological and optical properties of tin-antimony sulfide thin films synthesized by the spin coating method compared with ab initio calculation, *Mater. Lett.*, 2021, **300**, 130140, DOI: 10.1016/j.matlet.2021.130140.

59 S. Yuan, *et al.*, The effect of absorber thickness on the planar Sb_2S_3 thin film solar cell: Trade-off between light absorption and charge separation, *Sol. Energy*, 2021, **29**, 323–329, DOI: 10.1016/j.solener.2020.02.074.

60 M. I. Medina-Montes, Z. Montiel-González, N. R. Mathews and X. Mathew, The influence of film deposition temperature on the subsequent post-annealing and crystallization of sputtered Sb_2S_3 thin films, *J. Phys. Chem. Solids*, 2017, **111**, 182–189, DOI: 10.1016/j.jpcs.2017.07.035.

61 Z. Chen and G. Chen, The effect of absorber thickness on the planar Sb_2S_3 thin film solar cell: Trade-off between light absorption and charge separation, *Sol. Energy*, 2020, **201**, 323–329, DOI: 10.1016/j.solener.2020.02.074.

62 E. Aslan and M. Zarbali, Preparation of high-performance Sb2S3-based visible-light photodetector with excellent reversibility, *Opt. Mater.*, 2022, **133**, 113028, DOI: 10.1016/j.optmat.2022.113028.

63 A. N. Kulkarni, *et al.*, Structural and optical properties of nanocrystalline Sb_2S_3 films deposited by chemical solution deposition, *Opt. Mater.*, 2015, **46**, 536–541, DOI: 10.1016/j.optmat.2015.04.066.

64 F. Cao, *et al.*, Well-defined Sb2S3 microspheres: High-yield synthesis, characterization, their optical and electrochemical hydrogen storage properties, *Solid State Sci.*, 2011, **13**(6), 1226–1231, DOI: 10.1016/j.solidstatesciences.2011.02.007.

65 Y. Liu, D. M. Li, J. Qian, B. Di, G. Zhang and Z. H. Ren, Electrical impedance spectroscopy (EIS) in plant roots research: a review, *Plant Methods*, 2021, **17**(1), 1–25, DOI: 10.1186/s13007-021-00817-3.

66 H. D. E. Uygun and Z. O. Uygun, in Electrochemical Impedance Spectroscopy (EIS) Principles and Biosensing Applications, *Handbook of Nanobioelectrochemistry: Application in Devices and Biomolecular Sensing*, 2023, pp. 919–939, DOI: 10.1007/978-981-19-9437-1_42.

67 J. He, P. Liu, R. Ran, W. Wang, W. Zhou and Z. Shao, Single-atom catalysts for high-efficiency photocatalytic and photoelectrochemical water splitting: distinctive roles, unique fabrication methods and specific design strategies, *J. Mater. Chem. A*, 2022, **10**(13), 6835–6871, DOI: 10.1039/d2ta00835a.

68 D. Liu, *et al.*, Constructing 1D/0D $Sb_2S_3/Cd_{0.6}ZnSb_2S_3S$ S-scheme heterojunction by vapor transport deposition and in-situ hydrothermal strategy towards photoelectrochemical water splitting, *J. Alloys Compd.*, 2024, **975**, 172926, DOI: **10.1016/j.jallcom.2023.172926**.

69 C. Chailuecha, R. Sirirak, T. Suriwong and A. Klinbumrung, Impact of Controlled Thermal Oxidation on Phase Transition and Tailoring Properties of Sb_2S_3/Sb_2O_3 Composites, *Met. Mater. Int.*, 2024, **30**(11), 3069–3081, DOI: **10.1007/s12540-024-01692-y**.

70 A. S. Altowyan, M. Shaban, K. Abdelkarem and A. M. El Sayed, The Influence of Electrode Thickness on the Structure and Water Splitting Performance of Iridium Oxide Nanostructured Films, *Nanomaterials*, 2022, **12**(19), 1–13, DOI: **10.3390/nano12193272**.

71 A. D. Deangelis, K. C. Kemp, N. Gaillard and K. S. Kim, Antimony (III) sulfide thin films as a photoanode material in photocatalytic water splitting Center for Superfunctional Materials, Department of Chemistry, Ulsan National Institute of Center for Superfunctional Materials, Department of Chemistry, Po, Iii, 2016, DOI: **10.1021/acsami.5b12178**.